A&A 431, 253–268 (2005)
DOI: 10.1051/0004-6361:20040530

Astronomy & Astrophysics

The structure and dynamics of the dense cores in the Perseus molecular cloud complex

L. Olmi[1], L. Testi[2], and A. I. Sargent[3]

[1] Istituto di Radioastronomia, Largo E. Fermi 5, 50125 Firenze, Italy
e-mail: olmi@arcetri.astro.it
[2] Osservatorio Astrofisico di Arcetri, Largo E. Fermi 5, 50125 Firenze, Italy
e-mail: ltesti@arcetri.astro.it
[3] Department of Astronomy, California Institute of Technology, MC 105-24, Pasadena, CA 91125, USA

Received 26 March 2004 / Accepted 15 October 2004

Abstract. We have produced wide-field ($\gtrsim$0.1 deg^2) images of the molecular gas around the dense cores observed by Ladd et al. (1994) in the Perseus cloud complex in various CO (CO(1–0), ^{13}CO(1–0), C^{18}O(1–0)) and CS (CS(2–1), C^{34}S(2–1)) isotopomers, and N_2H^+(1–0), using the 16-element focal plane array operating at a wavelength of 3 mm at the Five College Radio Astronomy Observatory. We also performed mosaic observations in the N_2H^+(1–0) line and in the adjacent 3 mm continuum with the OVRO interferometer. Only within one of the observed cores we unambiguously detected a 3 mm continuum compact source with the interferometer. The single-dish large-scale maps of the densest gas, which in Perseus is concentrated within two large filamentary structures roughly aligned along a NE–SW axis, allowed us to analyse the spatial and kinematical properties of the cores and of the surrounding ambient gas. In the PER4/PER5 and PER7 regions we find that the large-scale and core velocity gradients have the same sign and similar magnitudes. In at least three cases we then find pairs of nearby cores with differences in the CS and N_2H^+ emission and in the line profile, which may have been caused by evolutionary effects. The small fraction of cores with compact continuum sources, the chemical differentiation and the inward motions observed suggest that we are observing objects in a phase preceeding the collapse and the formation of stars.

Key words. ISM: molecules – stars: formation – radio lines: ISM

1. Introduction

In recent years there has been a considerable attention to the initial phases of the star formation process, particularly the phases preceeding the core collapse and the formation of a young protostar. This interest was partly motivated by the possible link observed between the cloud fragmentation processes and the stellar initial mass function (Testi & Sargent 1998; Motte et al. 1998), and more generally by the attempt to provide a global picture of the star formation process, its efficiency and timescales.

Two opposite views of the global process of star formation in molecular clouds have emerged: a *slow* or magnetically driven one (Shu et al. 1987; Palla & Stahler 2000) and a *fast* or turbulence driven one (Hartmann et al. 2001). Even if, in principle, these two views have radically different predictions on the behaviour of the star formation process, it has proven very difficult to provide unambiguous observational tests.

During recent years we have carried out an extensive millimeter wavelengths observational project aimed at the characterization of the physical and kinematical properties of star forming clouds on angular scales that span from the individual protostellar systems to that of the moderately dense gas clumps. The main goal is to provide observational benchmarks for the models to compare with. Results on the Serpens region have been presented in Testi et al. (2000) and Olmi & Testi (2002, OT, hereafter), here we report our results on the Perseus region.

The Perseus molecular cloud complex consists of several regions of high visual extinction extending over an area of about 9 by 9 degrees at a galactic longitude of ∼160° and latitude ranging from −23° to −14°. The question of the distance to the Perseus complex is still controversial, though the value adopted by most authors is 350 pc (Borgman & Blaauw 1964). In Perseus there are two main active sites of star formation, IC 348 (see, e.g., Bachiller et al. 1987) and NGC 1333 (see, e.g., Jennings et al. 1987) connected by a chain of colder dark clouds (e.g., B 1) which are active in forming low-mass stars. The complex contains also other well-studied regions of star formation activity, such as L1448, L1455 and B 5. The main two regions, NGC 1333 and IC 348 are bright and contain newly formed intermediate-mass stars of spectral type B, as well as a cluster of young stars of lower mass.

The Perseus molecular cloud is interesting because unlike the Taurus complex, where only T-Tauri stars are found, young stars with relatively high luminosity, as well as low-mass stars,

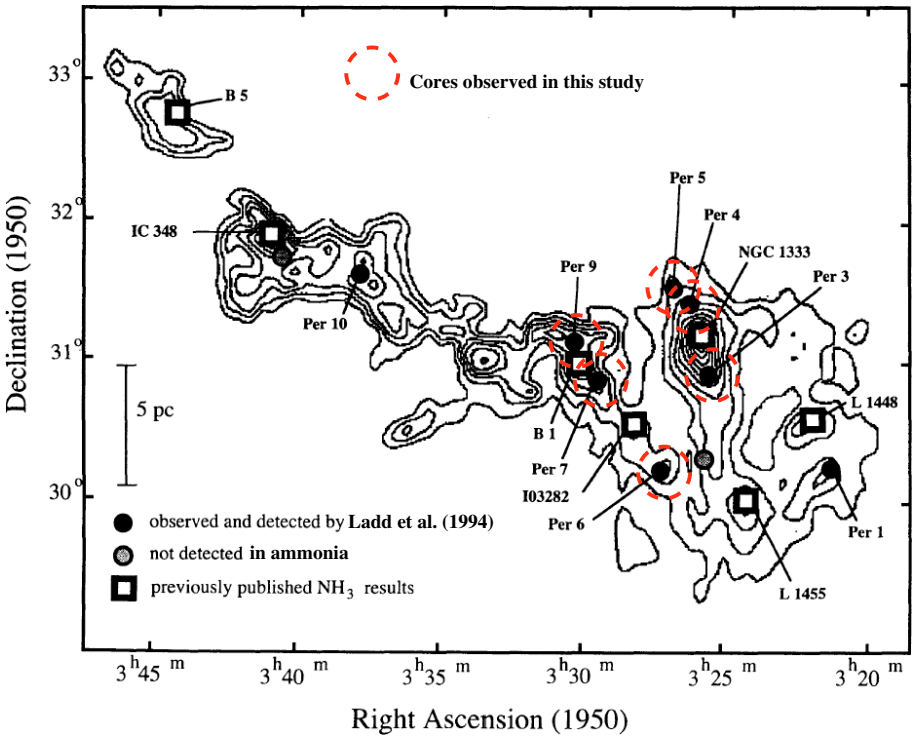

Fig. 1. Overview of the Perseus molecular cloud as observed in ^{13}CO(1−0), adapted from Ladd et al. (1994) and Bachiller & Cernicharo (1990); the locations of the cores studied in this paper are marked with dashed circles (Per 3, 4, 5, 6, 7, and 9).

are associated with the Perseus region. In fact, from an infrared study of the embedded young stars and an NH_3 survey, Ladd et al. (1993, 1994) concluded that the mean properties of Perseus are intermediate between those of Taurus, whose cores are less massive and more quiescent, and those of Orion A, whose cores are more massive and more turbulent.

The whole Perseus molecular cloud complex has been mapped in ^{13}CO(1–0) with 5′ resolution by Bachiller & Cernicharo (1986). Although parts of the Perseus complex had been searched for NH_3, the work by Ladd et al. (1994) was the first systematic, cloudwide study of the dense material around young IRAS sources in the Perseus region, producing wide-field NH_3(1, 1) maps up to 5′ × 15′. Subsequent high-resolution, wide-field line and continuum studies have been limited mostly to NGC 1333 (e.g., Warin et al. 1996; Sandell & Knee 2001) and a few cores (Caselli et al. 2002). In this paper we present the results of the first systematic multi-line, multi-isotope study throughout the complex. Our goal was to produce wide-field ($\gtrsim$0.1 deg^2) images of selected areas of the Perseus complex, using various molecular gas tracers, to determine the spatial and kinematical properties of the cores and the surrounding ambient gas (in the following, the term "core" will be used to indicate the densest regions of the molecular gas, probed by high-density tracers, whereas "cloud" or "clump" will indicate a larger region in which the cores are embedded). The inner regions of many cores were mapped interferometrically to derive information on the small-scale structure and to search for protostars. In Fig. 1 we show an overview of the Perseus molecular cloud, adapted from Ladd et al. (1994) and Bachiller & Cernicharo (1990), on top of which we indicate the cores subject of this study.

The paper is organized as follows: in Sect. 2 we describe the observations; in Sect. 3 we present our results and describe the morphology of the Perseus cloud and cores and their kinematics properties; in Sect. 4 we discuss the results and derive the physical conditions of the molecular gas; finally, in Sect. 5 we summarize the main results of this study.

2. Observations

2.1. FCRAO observations

The single dish observations of the Perseus cloud cores were carried out between April 1999 and June 2000 with the 13.7-m telescope of the Five College Radio Astronomy Observatory[1] (FCRAO) located in New Salem (USA), using the new SEQUOIA 32 element focal plane array, although only 16 pixels were actually operational during our observations. Many of the observed spectra could not be utilised because of bad weather. As a consequence some of our maps show blank areas were blocks of spectra had to be rejected and could not be re-observed. Though incomplete these maps are presented here because they provide useful informations and also give indications for follow-up observations of these regions.

The observed lines and their rest frequencies are listed in Table 1. The FWHM of the FCRAO telescope varied from about 46″ to about 53″. The front-end receivers employed low noise InP MMIC-based amplifiers resulting in a mean receiver temperature of 70 K (SSB) and system

[1] The Five College Radio Astronomy Observatory is operated with support from the National Science Foundation and with permission of the Metropolitan District Commission.

Table 1. Molecular transitions observed and their rest frequencies. The third column lists the cores where the transition has been observed.

Line	Frequency [GHz]	Observed cores with FCRAO
CS(2–1)	97.980968	PER3, PER4, PER5
		PER6, PER7, PER9
$C^{34}S(2–1)$	96.412982	PER7
$N_2H^+(1_{23}–0_{12})$	93.1734796	PER3, PER4, PER5
		PER6, PER7, PER9
CO(1–0)	115.271203	PER4, PER7
$^{13}CO(1–0)$	110.201353	PER3, PER4, PER5
		PER7
$C^{18}O(1–0)$	109.782182	PER3, PER4, PER5
		PER7

Table 2. Angular and linear size (FWHP, deconvolved) of the N_2H^+ cores (using a distance of 350 pc). Positions are (B1950).

(0, 0) position	Core	Offsets [arcsec]	θ_s [arcsec]	D_s [pc]
$03^h25^m39.2^s$	PER3-A[b,c]	(88, 178)	142	0.24
30°55′20″	PER3-B1	(−179, −81)	85	0.14
	PER3-B2	(−44, 44)	108	0.18
	PER3-B[a]	–	139	0.24
	PER3-C	(−176, 309)	74	0.12
$03^h26^m16.8^s$	PER4-A	(0, 151)	81	0.14
31°23′13″	PER4-B	(0, 0)	65	0.11
	PER4-C	(−88, 310)	148	0.25
	PER4-D	(44, −310)	92	0.16
$03^h26^m45.5^s$	PER5	(0, 0)	92	0.16
31°28′48″				
$03^h27^m10.3^s$	PER6-A	(0, 0)	90	0.15
30°13′04″	PER6-B[b,c]	(−88, 0)	58	0.10
$03^h29^m30.3^s$	PER7-A	(−88, −44)	100	0.17
30°49′50″	PER7-B	(88, 0)	89	0.15
	PER7-C	(−88, 133)	68	0.12
$03^h30^m19.6^s$	PER9-A	(88, 0)	97[b]	0.16
31°10′14″	PER9-B	(−178, 0)	77	0.13

[a] Using the B_1 50% contour level and including the B_2 core in the area of emission.
[b] Using the integrated emission within the contour at 65%.
[c] CS core.

temperatures typically comprised in the range 160−250 K. Our spectrometer was an autocorrelator with 24 KHz (i.e., 0.077 km s^{-1} at the N_2H^+(1–0) frequency) spectral resolution and 20 MHz bandwidth.

The integration times used for the single-scan were typically 4 to 15 min in frequency switching mode, using a frequency throw of 8 MHz. The maps were carried out in most cases using 1-beam sampling. The main beam efficiency used to convert the antenna temperature, T_A^*, to main beam brightness temperature is $\eta_{mb} = 0.55$. The final achieved sensitivities in the T_A^* scale varied from about 0.03 K for $C^{34}S$ to about 0.39 K for CO. Our source list is based on the Perseus cores observed in NH_3(1, 1) by Ladd et al. (1994). The coordinates of the (0, 0) position for each core are listed in Table 2.

2.2. OVRO observations

Using the OVRO Millimeter Array we have mapped, in the N_2H^+(1–0) line and in the adjacent 3 mm continuum, six ammonia cores peaks (see Table 2) from the the sample of Ladd et al. (1994). The six OVRO 10.4 m dishes have a primary beam of ∼75″ at the observing frequency, requiring several pointings to cover all the region of interest in the mapped cores. For each region we thus performed mosaic observations in order to obtain a uniform sensitivity over the area imaged at high angular resolution; the number of pointings per mosaic varied from 7 to 24 depending on the area of the core to be mapped. All the pointings in each mosaic where observed during the same source transit in order to ensure a uniform calibration across each mosaiced region.

Three configurations of the six antennas provided, for each mosaic, baselines from the shadowing limit (10.4 m) to ∼240 m. This (u, v) sampling ensures good sensitivity up to spatial scales of ∼30″ equivalent to 0.05 pc, or 10 300 AU, at the distance of Perseus (350 pc). Nevertheless, the interferometer recovered only a small fraction of the flux measured by the single-dish, as it will become evident in Sect. 3.2. All telescopes were equipped with cryogenically cooled SIS receivers which provided average system temperatures of ∼350 K (SSB) at the observing frequency. Continuum observations centered at 95 GHz were made in both (USB and LSB) 1 GHz wide bands of the analog correlator. An 8 MHz wide band, with a 0.083 MHz resolution, of the digital correlator was centered on the $N_2H^+(1_{23}–0_{12})$ transition at 93.1738 GHz (Caselli et al. 1995) at the Perseus velocity, $V_{LSR} \simeq 7.0$ km s^{-1}. Gain and phase were calibrated through frequent observations of the quasar 0333+321. 3C 273 and/or 3C 454.3 were used for passband calibration. The flux density scale was determined by observing Neptune and Uranus and the estimated uncertainty is less than 20%. All calibration and editing of the raw data have been performed with the MMA software package (Scoville et al. 1993). The calibrated (u, v) data were then imported in the GILDAS package for mosaic imaging and deconvolution (Gueth et al. 1996). The synthesized beam is approximately 6.″5 × 4.″0 FWHM in all maps, corresponding to a linear resolution ≤0.01 pc, or 2000 AU, and the noise level (for continuum observations) is ∼1−1.5 mJy/beam.

3. Results

3.1. Single-dish integrated intensity maps and line spectra

It was previously found by Ladd et al. (1994, LMG hereafter), using the NH_3(1, 1) line at 1.3 cm, that many of the NH_3 cores in Perseus were located along two high-density ridges (4−6 pc in extent), one centered on the NGC 1333 region and another extending SW from the B 1 core. These two ridges are also

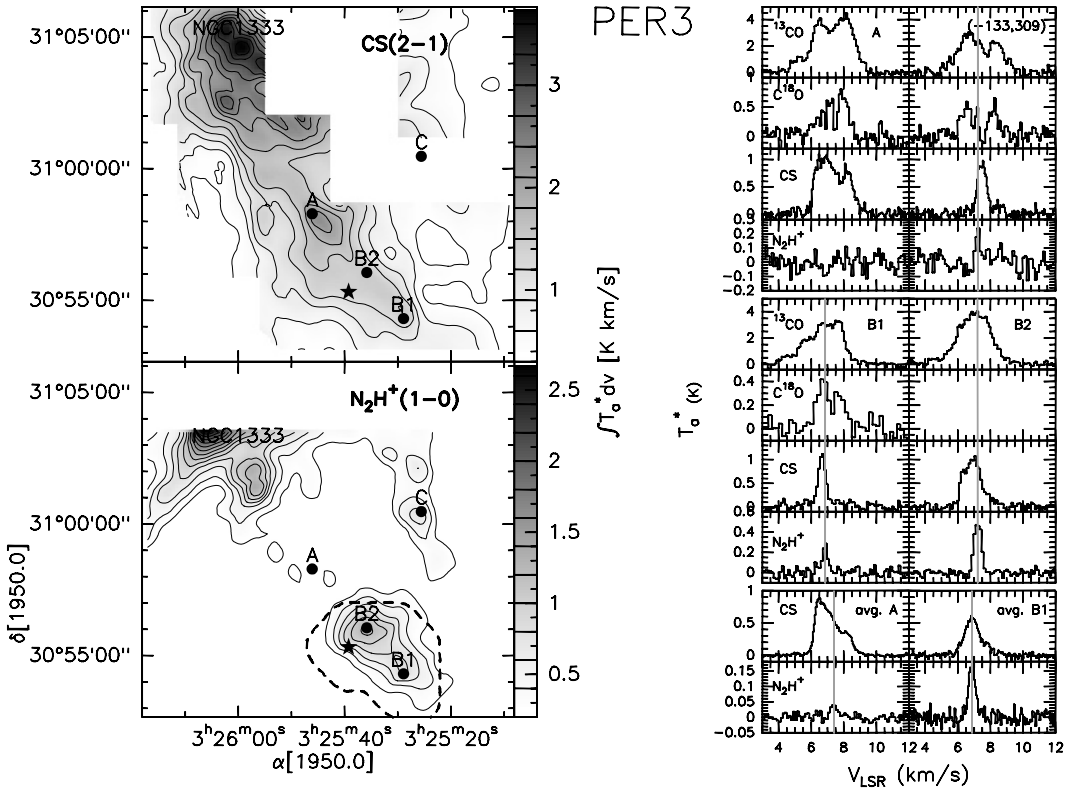

Fig. 2. *Left*: maps of the CS(2–1) and N_2H^+(1–0) integrated intensity in PER3. The value of the first contour and the contour interval are both 0.3 and 0.2 K km s^{-1}, respectively. The values of the contour levels are indicated in the wedge adjacent to each map. The star marks the IRAS source and reference position (see Table 2). The letters mark the positions of the main N_2H^+ and CS cores. The dashed contour indicates the area mapped by OVRO. *Right*: line spectra at the position of the various N_2H^+ and CS cores. Line spectra obtained by averaging the spectra contained in a 3 × 3 map centered around positions A and B_1 are also shown. Vertical lines are drawn at the peak velocities of the N_2H^+ Gaussian fits.

clearly visible in our global maps (not shown here for brevity), where the spatial distribution of the high-density molecular gas and of the dense cores is not random, but instead they are located within two large filamentary structures roughly aligned along a NE-SW axis. We now briefly comment the structure of each individual core.

3.1.1. PER3

PER3 shows two main cores, B_1 and B_2, which appear clearly separated in the N_2H^+ map of Fig. 2 (here and in the successive figures we show the integrated intensity of the main N_2H^+ hyperfine group, i.e. the $F_1, F = 2, 1-1, 1$, $F_1, F = 2, 3-1, 2$, and $F_1, F = 2, 2-1, 1$ components, whereas the line spectra show the $F_1, F = 0, 1-1, 2$ isolated component). Their line velocities are also different by almost as much as the line FWHM, as shown by Table 5 and Fig. 2. These features seem to suggest that B_1 and B_2 are two separate cores, rather than being part of a single core with a velocity gradient. Two separate peaks of emission towards PER3-B have also been observed by LMG in the $NH_3(1, 1)$ line.

There is no two-core morphology in the CS(2–1) line map, which shows an almost constant emission plateau at the positions of B_1 and B_2. The CS(2–1) line shows instead a peak of emission at position A, located between PER3 and NGC 1333 to the North-East, where there is almost no N_2H^+ emission, as shown in Fig. 2.

CS(2–1) spectral line profiles are mostly symmetric around core B_1 but become progressively more blue-asymmetric moving NE towards core A and the NGC 1333 region, as shown in Fig. 2. This is even more evident in the average line profiles of CS and N_2H^+ around cores A and B_1. Clearly, core A is characterized by very little N_2H^+ emission and a blue-asymmetric CS line profile, whereas the N_2H^+ core B_1 shows an average symmetric CS line profile whose peak is aligned with the peak of the N_2H^+ spectrum. We shall find a similar morphology also in cores PER6 and PER9 (see Sect. 4.1).

3.1.2. PER4

Our N_2H^+ map (see Fig. 3) clearly shows the two-arm structure of PER4 (see LMG and Caselli et al. 2002; CBMT, hereafter), one to the North and the other directed to the NE. The two arms are populated with several N_2H^+ cores, which only partially overlap with the CS cores. The CS diffuse emission roughly follows the morphology observed in the N_2H^+ line. The NH_3 map of LMG shows only the main arm to the North, with most of the emission coming from cores B and C. The

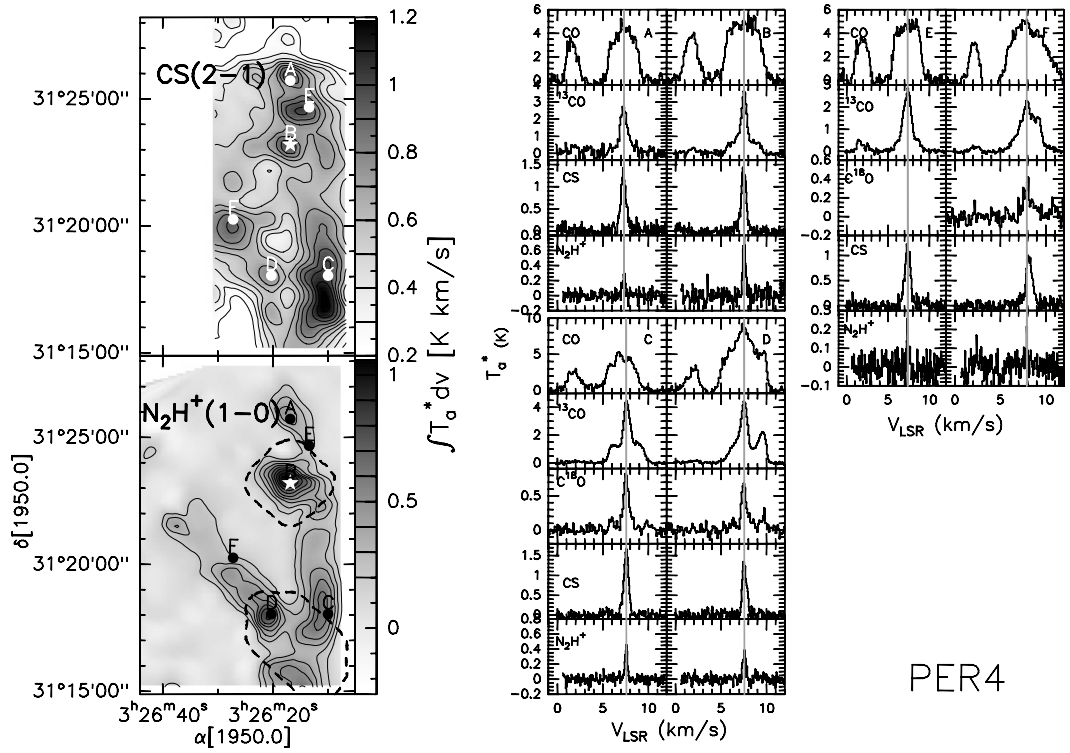

Fig. 3. *Left*: maps of the CS(2–1) and N_2H^+(1–0) integrated intensity in PER4. The value of the first contour is 0.2 K km s^{-1} and the contour interval is 0.1 K km s^{-1} for both N_2H^+ and CS. The values of the contour levels are indicated in the wedge adjacent to each map. The star marks the IRAS source and reference position (see Table 2). The letters mark the positions of the main N_2H^+ and CS cores. The dashed contour indicates the area mapped by OVRO. *Right*: line spectra at the position of the various N_2H^+ and CS cores. Vertical lines are drawn at the peak velocities of the N_2H^+ Gaussian fits.

southernmost CS and N_2H^+ emission is coincident with a region where there is bulk emission from both ^{13}CO and C^{18}O, originating from the NGC 1333 region (Warin et al. 1996).

In Fig. 4 we show the structure of the large-scale gas, traced by the CO(1–0) and ^{13}CO(1–0) emission, in three different velocity channels. Clearly, the N_2H^+ and CS cores are located in a region of enhanced CO, ^{13}CO (and C^{18}O, not shown) emission visible in the central velocity channel.

CS line profiles, though not perfectly Gaussian, do not show any clear blue-asymmetry, and their peak of emission is aligned with that of N_2H^+. The CS and N_2H^+ peaks are also aligned with the peak of emission of the C^{18}O(1–0) and ^{13}CO(1–0) lines, though in the case of the two CO isotopomers the line profile shows a strong peak superimposed on a larger plateau of emission, particularly in the case of ^{13}CO as shown in Fig. 3. The strong peak of emission in the CO isotopomers is clearly responsible of the enhanced region of emission previously described and further analysis is required to understand whether it could be consistent with the expections of an empyrical colliding-cloud scenario originally proposed by Loren (1976).

The CO and ^{13}CO spectra also show an isolated velocity component (at $V_{LSR} \simeq 2$ km s^{-1}) along the line of sight, which extends on almost the entire region mapped by us in CO towards PER4. Because the line profile of this component is quite isolated from the main velocity range where CO and ^{13}CO emission occurs, it seems plausible that the molecular gas responsible for this low-velocity emission is unrelated to PER4 and NGC 1333 and it is not a result of overlapping of various velocity components even in the hypothetical colliding-cloud scenario.

3.1.3. PER5

The PER5 molecular core is located NE of PER4 and is part of the long molecular ridge centered on NGC 1333. As shown in Fig. 5 PER5 is an isolated core where the peaks of emission in CS and N_2H^+ are spatially coincident and are centered on the IRAS source. The compactness of this core has been previously observed also by LMG and by CBMT. In contrast, our maps of the ^{13}CO(1–0) and C^{18}O(1–0) emission show a very different spatial distribution with an overall depression toward the N_2H^+ core. Although excitation and optical thickness effects cannot be entirely excluded, the different morphology in the various tracers observed by us might indicate that the CO isotopomers are depleted toward the dense core (e.g., Caselli et al. 1999; Bergin et al. 2002).

The molecular line profiles show that all tracers are spectrally aligned and the CS spectrum shows some minor line wings due to the presence in PER5 of a NS velocity gradient (see Sect. 3.3.2). However, the CS spectra do not show any blue-asymmetry in the region mapped by us around PER5 (see Fig. 5).

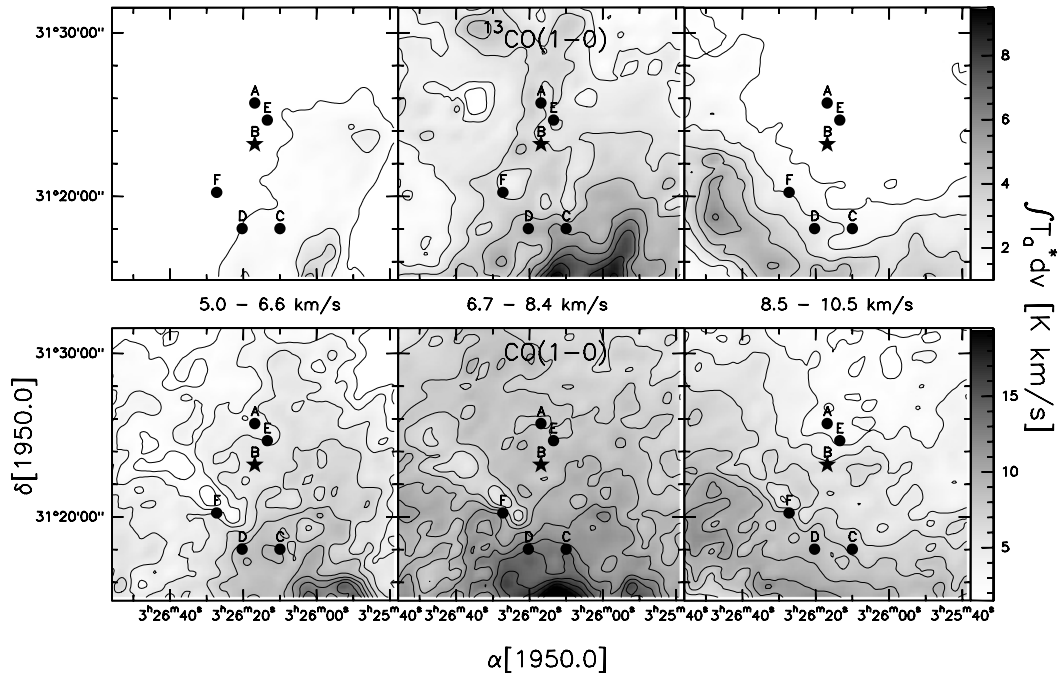

Fig. 4. Maps of the CO and ^{13}CO integrated intensity in PER4, in three velocity intervals: 5 to 6.6 km s^{-1}, 6.7 to 8.4 km s^{-1}, and 8.5 to 10.5 km s^{-1}. The value of the first contour and the contour interval are both 1.0 K km s^{-1} and 1.5 K km s^{-1}, in the ^{13}CO and CO maps, respectively. The star marks the position of the IRAS source as in Fig. 3.

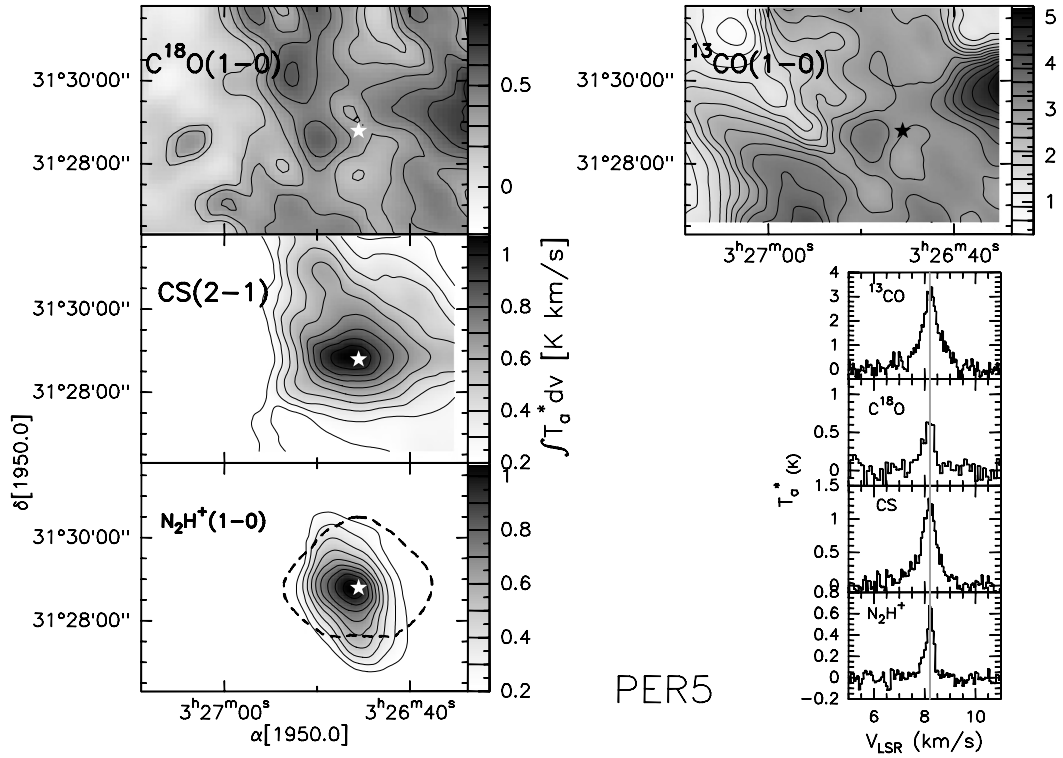

Fig. 5. *Left and top-right*: maps of the ^{13}CO(1–0), C^{18}O(1–0), CS(2–1) and N$_2$H$^+$(1–0) integrated intensity in PER5. The values of the contour levels are indicated in the wedge adjacent to each map. The star marks the IRAS source and reference position (see Table 2). The letters mark the positions of the main N$_2$H$^+$ and CS cores. The dashed contour indicates the area mapped by OVRO. *Bottom-right*: line spectra at the (0, 0) position. Vertical lines are drawn at the peak velocities of the N$_2$H$^+$ Gaussian fits.

3.1.4. PER6

The last three cores observed by us, PER6, PER7 and PER9 belong to the molecular ridge extending SW from the B 1 dark cloud. The maps of PER6 in Fig. 6 show an offset between the CS and N$_2$H$^+$ cores, which are otherwise spatially well defined, as well as an offset between the IRAS source and

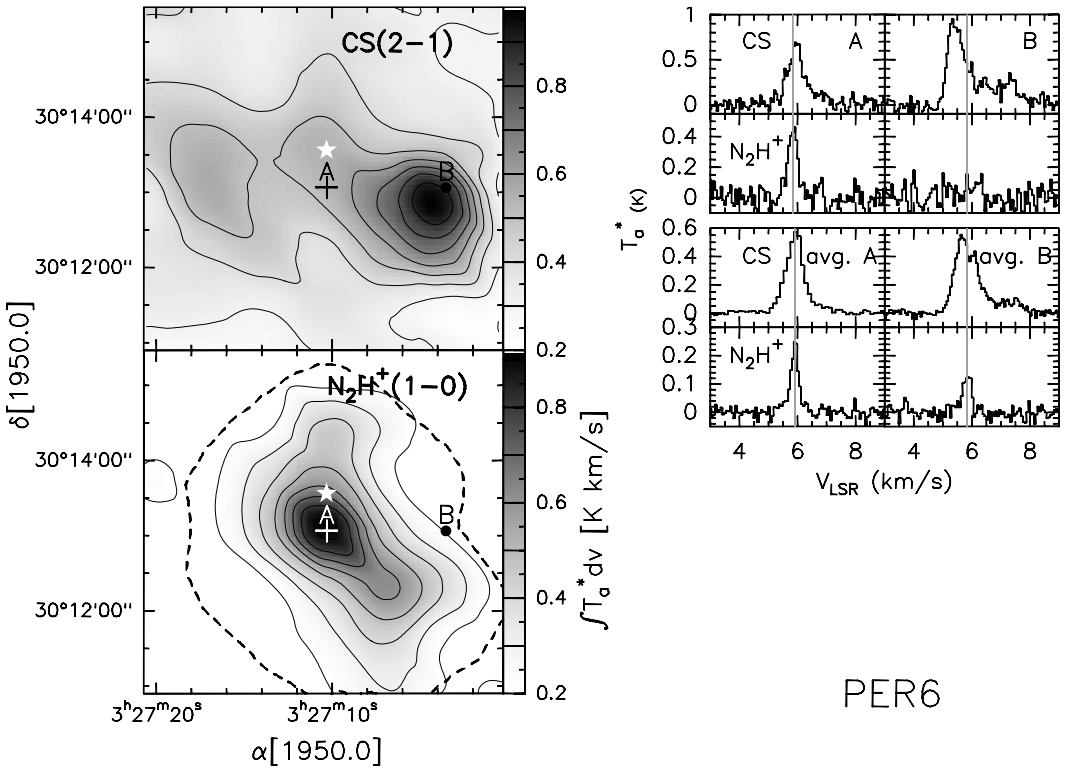

Fig. 6. *Left*: maps of the CS(2–1) and N_2H^+(1–0) integrated intensity in PER6. The values of the contour levels are indicated in the wedge adjacent to each map. The star marks the IRAS source and the cross marks the reference position (see Table 2). The letters mark the positions of the main N_2H^+ and CS cores. The dashed contour indicates the area mapped by OVRO. *Right*: line spectra at the position of the N_2H^+ and CS cores, A and B. Line spectra obtained by averaging the spectra contained in a 3 × 3 and 3 × 5 map centered around positions B and A, respectively, are also shown. Vertical lines are drawn at the peak velocities of the N_2H^+ Gaussian fits.

the molecular cores. The elongation of the N_2H^+ core along a NE–SW axis is also evident in the map of LMG.

As in the case of the PER3-A core, the CS line profiles around the position of core PER6-B, characterized by low N_2H^+ emission, show hints of a blue-asymmetric line shape (see Fig. 6). The asymmetry in the line profiles becomes more evident when averaging the spectra in a 3 × 3 map centered around position B, as shown in Fig. 6, where one can note that the mean N_2H^+ line profile has its peak almost aligned with the dip in the averaged CS spectrum. This is to be compared with the mean spectrum at position A, where the CS line profile is almost Gaussian and its peak is aligned with that of a stronger N_2H^+ line. These features are quite similar to those shown in Fig. 2 for the PER3 case.

3.1.5. PER7

PER7 is the next region on the B 1 ridge and is located about 13′ SW from B 1. The large-scale distribution of the molecular gas around PER7, as traced by $C^{18}O$(1–0) (not shown), shows that the densest molecular gas is distributed along a NE–SW axis, as already inferred by LMG using much smaller NH_3 maps. All dense cores observed by us, as well as the IRAS source, are located inside the ridge. The N_2H^+ map in Fig. 7 shows three main cores, labelled A, B and C, and it also shows the strong emission originating from B 1 to the NE. The spatial distribution of N_2H^+ follows quite closely (except for core C) the NH_3 map of LMG. The CS(2–1) map in Fig. 7 does not reproduce very well the distribution of the N_2H^+ cores, and the strongest emission in the $C^{34}S$ map comes from the position of core F, which does not have a corresponding N_2H^+ core.

The molecular line profiles in Fig. 7 show that the peaks of N_2H^+ and CS are usually aligned, and are also aligned with the peaks of $C^{34}S$ and $C^{18}O$ at the positions where these tracers are available. The CS line profiles are quite different over the mapped region, showing Gaussian, blue asymmetric and red asymmetric spectra. Clearly, higher angular resolution, higher sensitivity maps are needed of this region to determine its kinematics.

The CO and ^{13}CO spectra show an isolated velocity component along the line of sight (see Fig. 7), which has a similar velocity ($V_{LSR} \simeq 2$ km s^{-1}) to that observed in the case of PER4 and PER5. Another isolated velocity component, associated with a smaller and denser core, is observed in both N_2H^+ and CS at a velocity of about 8 km s^{-1} (see Fig. 7) to the North of core F.

3.1.6. PER9

PER9 is located near the North edge of the B 1 molecular ridge. It is about 10′ North of B 1 and ≃22′ NE of PER7. The N_2H^+ map in Fig. 8 shows the presence of two well separated cores of emission, labelled A and B. We have only a few CS spectra around the position of the strongest N_2H^+ core,

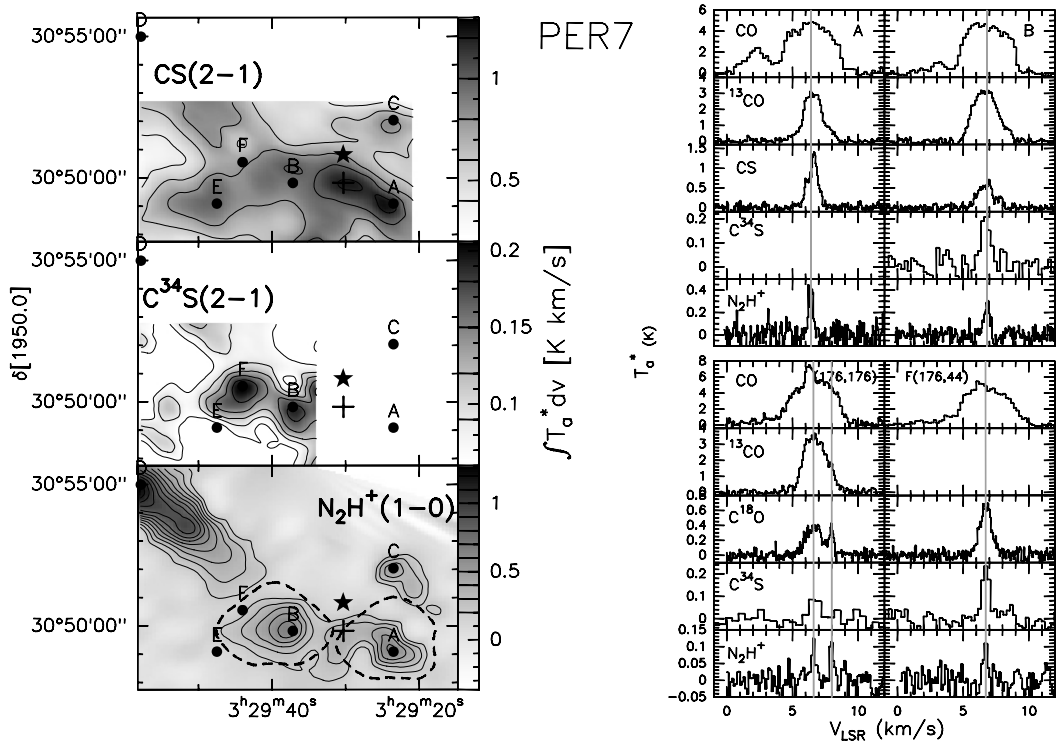

Fig. 7. *Left*: maps of the CS(2–1), $C^{34}S$(2–1) and N_2H^+(1–0) integrated intensity in PER7. The values of the contour levels are indicated in the wedge adjacent to each map. The star marks the IRAS source and the cross marks the reference position (see Table 2). The letters mark the positions of the main N_2H^+ and CS cores. The dashed contour indicates the areas mapped by OVRO. *Right*: line spectra at the position of the A, B, (176, 176) and F(176, 44) N_2H^+ and CS cores. Vertical lines are drawn at the peak velocities of the N_2H^+ Gaussian fits.

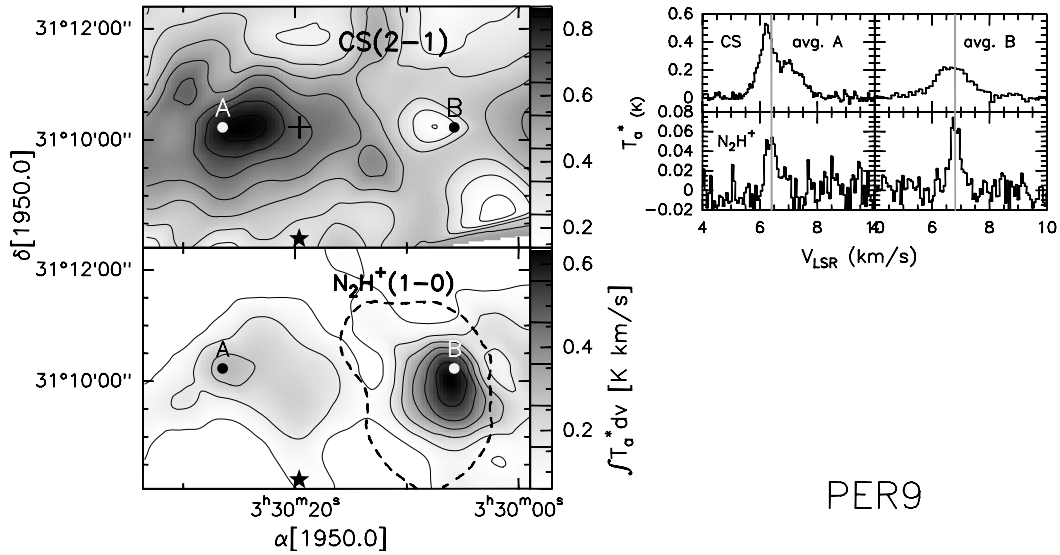

Fig. 8. *Left*: maps of the CS(2–1) and N_2H^+(1–0) integrated intensity in PER9. The values of the contour levels are indicated in the wedge adjacent to each map. The star marks the IRAS source and the cross marks the reference position (see Table 2). The letters mark the positions of the main N_2H^+ and CS cores. The dashed contour indicates the areas mapped by OVRO. *Right*: line spectra obtained by averaging the spectra contained in a 3×3 map centered around positions A and B are shown. Vertical lines are drawn at the peak velocities of the N_2H^+ Gaussian fits.

B, and thus the distribution of the CS gas around B shown in Fig. 8 is very approximate. However, the few CS spectra observed around B are enough to calculate the average spectrum, also shown in Fig. 8, and to note that CS emission is weaker at core B than it is at core A. The relative N_2H^+ intensity between the two cores is also well reproduced in the NH_3 map of LMG.

The mean spectra in Fig. 8 clearly show that the CS line profile is blue asymmetric toward core A but not around core B. We thus find yet another region in Perseus where the strongest CS condensation shows a significant blue excess in the spectrum and is associated with a core showing relatively little N_2H^+ emission, whereas the core where the CS emission is

less prominent shows no significant blue excess and is associated with a more intense N_2H^+ core.

3.2. OVRO maps

The results of our extensive interferometric mapping were largely negative, both in the line and continuum emission. This is not due to limited sensitivity, but rather to the lack of compact structures (density enhancements or protostars) within the observed cores. The continuum sensitivity of our observations was generally good and sufficient to detect dust condensations from a fraction to a few Solar masses, depending on the assumptions on the dust properties and physical conditions. The spatial resolution was well matched to the size of individual protostellar systems (a few thousand AUs) and the maximum scales to which the interferometer was sensitive are in the range 20″ to 40″.

We present a summary of our OVRO results in Fig. 9, where we show only sources with a well-defined N_2H^+(1–0) distribution. The N_2H^+ integrated intensity in the sources not shown in Fig. 9 was below the map 3σ level, which was ≃90 mJy/beam in PER3 and ≃600 mJy/beam in PER4 and PER5. Where detected, the N_2H^+ intensity peak observed with OVRO is not coincident with the peak of the integrated emission measured with the single-dish, particularly in the PER3 and PER4 cases. This is not surprising considering the different area of the sky sampled by the single-dish and interferometer beams and indicates that the emission of the diffuse, less dense gas is dominant compared to the emission coming from the localized denser regions imaged by OVRO. This is confirmed by the fact that the interferometer recovers only a small fraction of the flux measured by the single-dish, due to the lack of short-spacing information in the OVRO data. For example, in the PER5 case the total flux measured by OVRO in a ≃2.2 arcmin^2 area around the source is about 12.4 Jy, whereas the FCRAO flux measured in the same area and velocity interval is about 160 Jy. Thus, in this case OVRO recovers less than 10% of the total single-dish flux.

The continuum emission at 3 mm was unambiguously detected in PER5 only, where we measured 13.5 ± 5 mJy in an area of 143 arcsec^2. To convert a continuum flux into a mass we adopted an opacity $k_{1.3\ \mathrm{mm}} = 5 \times 10^{-3}$ cm^{2}g^{-1} and a spectral slope $\beta = 1.1$. Hence, we obtain a total gas+dust mass $M_{\mathrm{tot}} \simeq 2.2\ M_\odot$ if $T_{\mathrm{dust}} \simeq 10$ K or $M_{\mathrm{tot}} \simeq 1\ M_\odot$ if $T_{\mathrm{dust}} \simeq 20$ K, which are somewhat lower than the values shown in Table 6, discussed later. We should note, however, that M_{tot} has been obtained from a much smaller area.

We can conclude that the only cores showing evidence of compact structures and possibly protostellar or pre-protostellar objects are PER3-B1/B2, PER4-B, and PER5.

3.3. Kinematics of the Perseus region

The analysis of the gas kinematics in the Perseus region is complicated by the presence of multiple clumps along the line of sight and by several velocity fields that include infall, expansion, rotation and turbulence. Rotation is a common feature of dense cores in molecular clouds, as shown by Goodman et al. (1993). On the other hand, the presence of several molecular outflows in the Perseus cloud complex could also have affected the cloud kinematics. It is however difficult to give a quantitative estimate of the physical parameters that may measure the dynamical effects of the molecular outflows on the cloud.

Following Arce & Goodman (2003) one possible method consists of defining the "escape mass" (M_{esc}) as the mass that

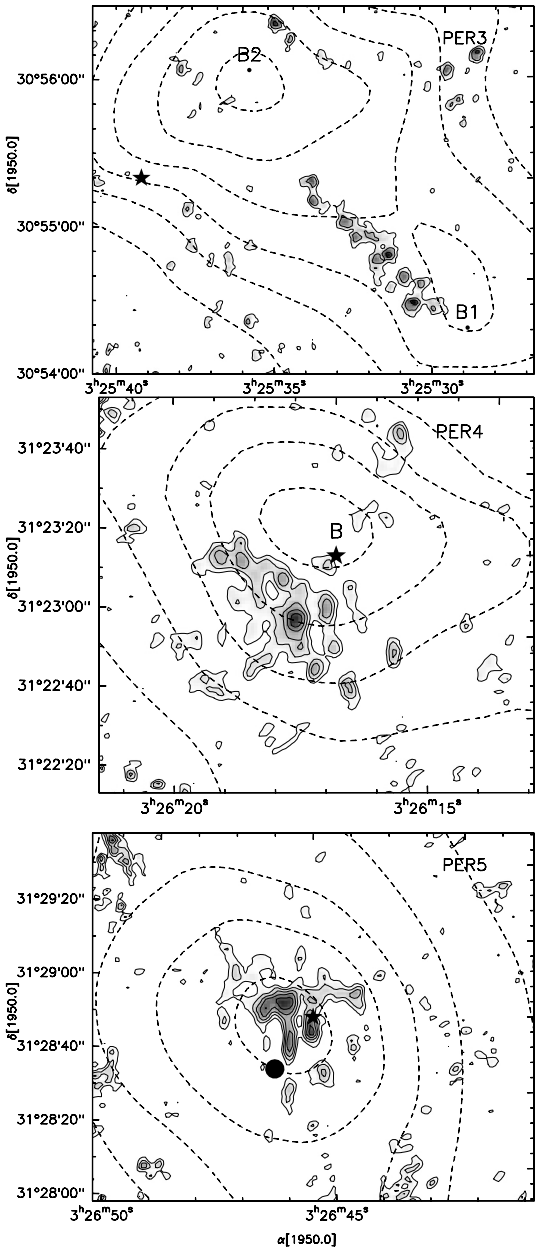

Fig. 9. OVRO maps of the N_2H^+ integrated (over all hyperfine components) intensity (grey scale and solid contours) in PER3, PER4 and PER5, superimposed on the FCRAO single-dish maps (dashed contours). In the OVRO images of PER3 the value of the first contour is 80 mJy/beam and the contour interval is 40 mJy/beam. In the images of PER4 and PER5 the first contour is 400 mJy/beam and the contour interval is 200 mJy/beam. The stars mark the positions of the IRAS sources, whereas the large dot in the map of PER5 corresponds to the 3 mm-continuum peak position.

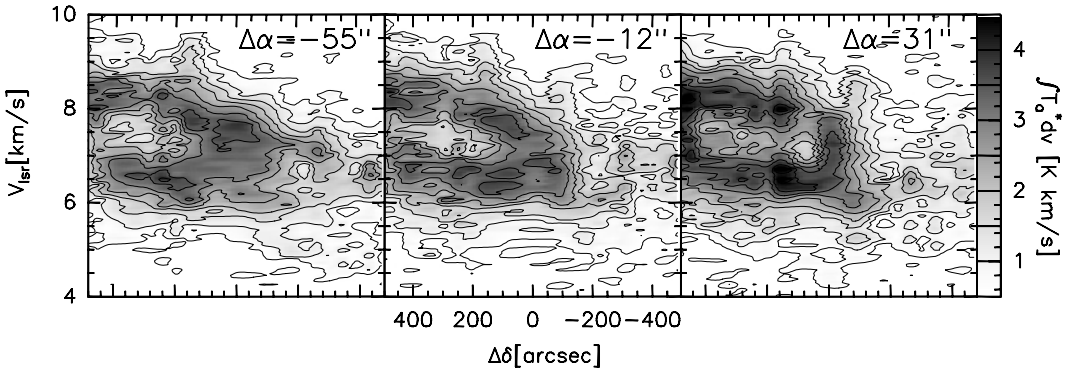

Fig. 10. Position-velocity channel map in PER3, using the ^{13}CO(1–0) line, for three offsets in right ascension, from left to right: −55″, −12″ and 31″. The coordinates offsets are relative to the reference position listed in Table 2.

could potentially be dispersed by an outflow, and thus represents a measure of the potential disruptive effect outflows may have on their cloud. The escape mass is then defined as $M_{\rm esc} = P_{\rm flow}/V_{\rm esc}$, where $P_{\rm flow}$ is the outflow momentum and $V_{\rm esc}$ is the cloud's escape velocity. As an example of application to Perseus we consider the cases of NGC 1333 and B 1. In the former, $V_{\rm esc} \simeq 1.7$ km s^{-1} (from the data compiled by LMG) and $P_{\rm flow} = 11\ M_\odot$ km s^{-1} (HH 7–11, from Bachiller & Cernicharo 1990). We thus obtain $M_{\rm esc} \simeq 6.5\ M_\odot$, *uncorrected* for projection effects. Likewise, in the B 1 case $V_{\rm esc} \simeq 0.7$ km s^{-1} and $P_{\rm flow} = 0.01\ M_\odot$ km s^{-1} (from Bachiller et al. 1990) and thus $M_{\rm esc} \simeq 0.02\ M_\odot$.

Therefore, given that the values quoted above are uncorrected for the inclination angle, it appears that the HH 7–11 outflow in NGC 1333 could actually have affected the ambient cloud's velocity and density distribution at parsec-scale distances from the source. However, the NGC 1333 and surrounding region is a crowded site of star formation and it is not thus clear what the outflow's effects would be at the distances of PER3 (1.2 pc), PER4 (1.4 pc) and PER5 (2.6 pc). On the other hand it seems unlikely that the outflow in B 1 may have any substantial effect on the parent cloud. In conclusion, although the most energetic molecular outflow in the NGC 1333 region may have affected the cloud kinematics at some level, in the following analysis it will still be useful to parameterize the observed velocity gradients as if they were caused by actual solid-body rotations.

3.3.1. PER3

In Fig. 10 we show the position(DEC)-velocity (PV, hereafter) diagram of ^{13}CO(1–0) at three selected RA offsets. One can note the peculiar "O" or reverse "C" shaped appearance of the three PV diagrams, i.e. an almost circular ring of emission with a hole in the middle. A similar "O" shaped feature is also observed in the P(RA)V diagram at DEC offsets between about 70″ and 300″ (not shown).

One possible interpretation of this "O" structure in the PV diagram is that we are observing the expansion, or contraction, along the line of sight of a nearly spherical shell surrounding a cavity characterized by a lower emission. Warin et al. (1996) have explained the spatial-velocity features of the NGC 1333 core as an expanding hollow spherical shell, generated by several ouflows whose sources are inside or near the cavity. However, it is unlikely that the "O" shaped feature in the PV diagrams of PER3 is also caused by outflows, as at our sensitivity level we do not find any sign of outflows associated with the PER3 region that would corroborate the expanding shell scenario.

The most likely explanation for the ^{13}CO PV diagrams of Fig. 10 is thus the overlapping along the line of sight of two clouds at different velocities. In fact, in the region where the "O" shaped feature of Fig. 10 is observed, the ^{13}CO(1–0) line is characterized by double-peaked spectra; it is unlikely that this is due to optical depth effects since also the optically thin C^{18}O(1–0) transition shows a line profile with two peaks at the same velocities as the more abundant isotopomer.

We have then searched for velocity gradients across core B of the PER3 region. A cloud undergoing solid-body rotation would exhibit a linear gradient, dV/dr, across the face of a map, perpendicular to the rotation axis (Goodman et al. 1993). The velocity gradient of an interstellar gas cloud can be determined by using all or most of the data in a map at once, by least-squares fitting maps of line-center velocity for the direction and magnitude of the best-fit velocity gradient. Following the same method as described by OT we can then fit a velocity gradient to PER3-B. Table 3 shows that the velocity gradient in PER3-B is dominated by core B$_2$ and is the highest measured by us in the Perseus cloud complex.

3.3.2. The PER4/PER5 region

The PER4/PER5 region is located at the North edge of the filamentary structure centered on NGC 1333. We have used the merged C^{18}O map of PER4 and PER5 to create a channel map and two PV maps of this region, shown in Figs. 11 and 12. Three interesting features can be noted in the case of the P(RA)V diagram shown in the bottom panels of Fig. 12: *(i)* in the southern part of the clump (left panel) we observe an EW velocity gradient; *(ii)* in the northern part of the clump (right panel) the velocity gradient is instead in the WE direction; *(iii)* finally, in the central part (i.e. ΔDec = −91″ in

Table 3. Results of velocity gradient fitting. The magnitude of the velocity gradient is represented by dV/dr, while θ_v represents the direction of increasing velocity, measured positive E of N. The LSR systemic velocity is V_0.

Clump	Line used	V_0	dV/dr	θ_v
		[km s^{-1}]	[km s^{-1} pc^{-1}]	[deg E of N]
PER3-B	N_2H^+(1–0)	7.36	2.32	88
PER3-B2	N_2H^+(1–0)	7.37	2.49	89
PER4-B	N_2H^+(1–0)	7.51	0.57	–67
PER4/PER5-SW	$C^{18}O$(1–0)	7.63	0.58	–79
PER4/PER5-NE	$C^{18}O$(1–0)	7.21	1.50	85
PER5	CS(2–1)	8.16	0.83	33
PER5	N_2H^+(1–0)	8.20	0.69	14
PER6-B	CS(2–1)	5.92	0.65	71
PER6-A	N_2H^+(1–0)	5.92	0.40	47
PER7	$C^{18}O$(1–0)	6.57	0.14	41
PER7[(a)]	N_2H^+(1–0)	6.66	0.75	25
PER9-B	N_2H^+(1–0)	6.45	0.94	70

[(a)] Across the region with the main cores, excluding B 1.

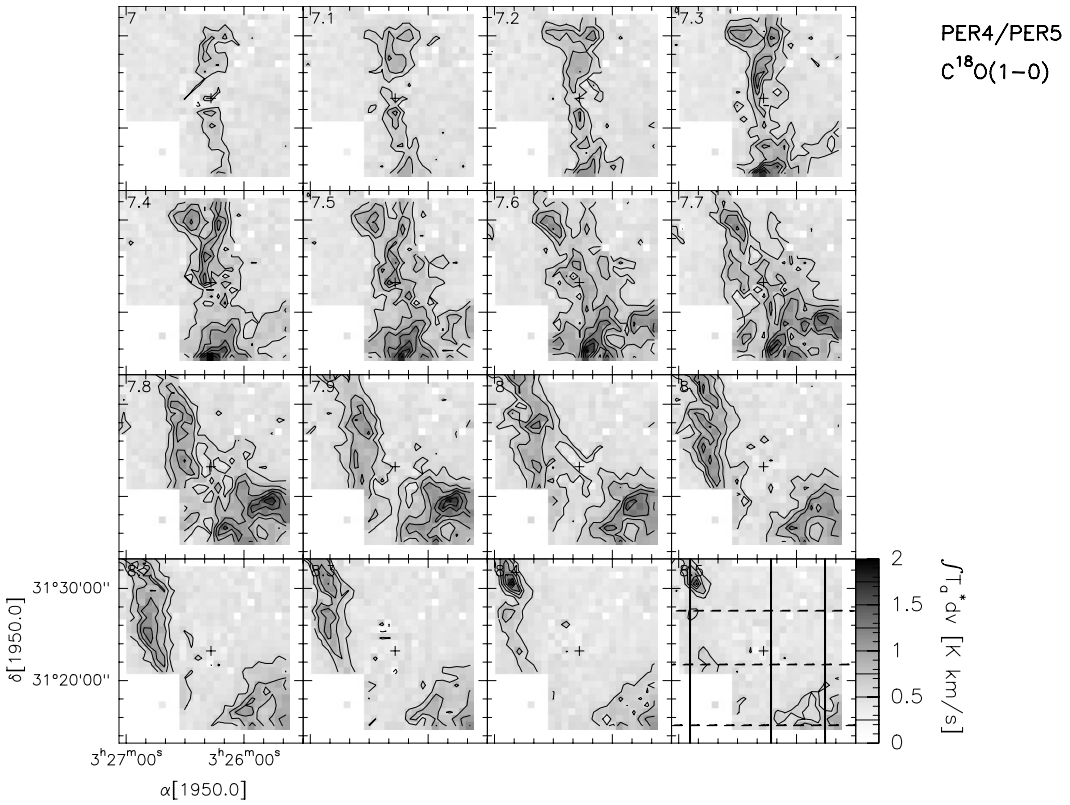

Fig. 11. Channel map of the $C^{18}O$ intensity in the PER4/PER5 region. The values of the contour levels are indicated in the wedge adjacent to the last channel. The velocity of each channel, in km s^{-1}, is indicated in the top-left corner of each map. The cross indicates the position $\alpha[B1950] = 03^h26^m16.8^s$ and $\delta[B1950] = 31°23'13''$. The (solid) vertical and (dashed) horizontal lines in the last panel indicate the sections corresponding to the position(Dec)-velocity (vertical lines) and position(RA)-velocity (horizontal lines) maps shown in Fig. 12.

Fig. 12) we have an overlapping of both velocity gradients, resulting in a V-shaped PV diagram.

The PV diagram and the $C^{18}O$ channel map in Fig. 11 suggest the presence of two separate $C^{18}O$ clumps, one of which is mostly confined to the NE while the other is concentrated in the SW of the PER4/PER5 region. The two clumps overlap in a region located approximately around the PER4 cores A, B and E. Most of the PER4 cores are located at this cloud-cloud interface, whereas the PER5 core belongs to the NE clump. In one possible scenario the observed velocity gradients are associated

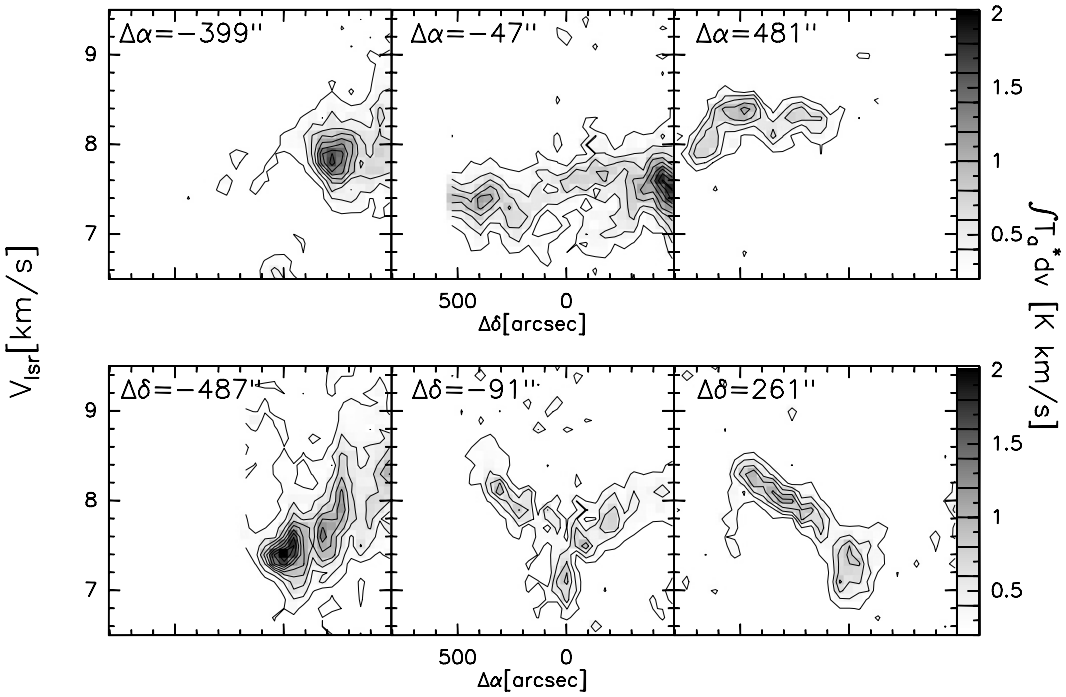

Fig. 12. *Top*: position(Dec)-velocity channel map in the PER4/PER5 region, using the $C^{18}O$(1–0) line, for three offsets in right ascension, from left to right: −399″, −47″ and 481″. *Bottom*: position(RA)-velocity channel map in the PER4/PER5 region, using the $C^{18}O$(1–0) line, for three offsets in declination, from left to right: −487″, −91″ and 261″. The coordinates offsets are relative to the reference position marked by the cross in Fig. 11. The values of the contour levels are indicated in the wedge adjacent to each PV plot. The map sections used for the PV plots are also shown in Fig. 11.

with rotational motions, in which case the NE and SW clumps appear to have opposite sense of rotations and overlap at the cloud-cloud interface.

This scenario is corroborated by the P(DEC)V diagrams in the top panels of Fig. 12. Here, the emission is confined at low declinations in the negative RA offset (left panel), whereas at extreme positive RA offsets (right panel) the emission comes mostly from higher declinations. In the middle panel ($\Delta\alpha = -47''$) the emission comes from a wider range of declinations. Moreover, in all three PV diagrams the emission is mostly confined to a horizontal strip with approximately constant velocity, though with different values. The latter are higher (∼8−8.4 km s^{-1}) at the two extreme RA offsets, whereas the typical velocity is lower (≃7.4 km s^{-1}) in the middle panel. Though it is not a unique explanation, all these spatial-velocity features could be explained by the existence of two clumps, one in the SW and the other in the NE of the PER4/PER5 region, with opposite senses of rotation. If the axis of rotation of both clumps is roughly aligned in the NS direction and if there exist a RA offset between them, both PV diagrams can be explained simultaneously. Clearly, there are a number of alternative interpretations, such as expanding filaments, shear motions and multiple cloud components, and our data cannot be used to discriminate among these various scenarios.

By applying to the $C^{18}O$ map the same velocity gradient fitting method as described by OT we can fit a velocity gradient separately to the SW and NE clumps of the PER4/PER5 region. The results are shown in Table 3 and confirm that the two clumps exhibit opposite velocity gradients.

As far as the individual cores in the PER4/PER5 region are concerned, it was of interest to search for velocity gradients across the most prominent cores and compare them with the large-scale gradients described above. In PER4 we have searched for velocity gradients across the N_2H^+ core PER4-B. As shown in Table 3 the direction and magnitude of the velocity gradient are quite similar to those associated with the large-scale increment of velocity observed in the SW clump of the overall PER4/PER5 region.

In the isolated PER5 core the P(DEC)V diagrams of both N_2H^+ and CS show the presence of a velocity gradient which is mostly oriented NS. A more quantitative fit gives a direction of the velocity gradient of about 33° and 14° for CS and N_2H^+, respectively, i.e. increasing in the N–NE direction (see Table 3). Although the direction of the gradient across the core and that of the large-scale molecular gas (PER4/PER5-NE in Table 3) belong to the same quadrant, they differ by more than 50° and it is thus unclear whether there may be any physical connection between them.

3.3.3. PER6, PER7 and PER9

PER6 shows two distinct regions of emission, in CS and N_2H^+. As in the case of the isolated PER5 core we have searched for velocity gradients across the two condensations. By using both molecular gas tracers, CS(2–1) and N_2H^+(1–0), we were able to find a moderate increment of the velocity in approximately the SW–NE direction, as shown in Table 3. Thus, the direction of the velocity gradient is consistent with the large-scale

velocity gradient observed in the region using $C^{18}O(1–0)$, as discussed below.

PER7 represents the only region located on the molecular ridge extending SW from the B 1 core for which we have maps of the large-scale distribution of the molecular gas. It is thus of interest to compare the kinematics of the B 1 and NGC 1333 ridges. Of all observed CO isotopomers only $C^{18}O$ can effectively be used to determine the presence of large-scale velocity gradients in the map. By applying to the $C^{18}O$ map the same velocity gradient fitting method as described by OT we find an increasing velocity in the SW–NE direction (see Table 3), i.e. roughly the same direction as the filamentary structure containing the cores.

The CS(2–1) channel map and PV diagrams show that the PER7 cores visible in Fig. 7 are at different velocities and we also find a velocity gradient across the main cores with a direction close to the WE axis (if emission from the B 1 region is not included in the computation). Interestingly, this velocity increment has a direction which differs by more than 100° with that observed in B 1. However, the latter was not a target of this work and thus has not been properly sampled. An isolated velocity component at $V_{\rm LSR} \simeq 2$ km s^{-1} is also visible in the ^{13}CO and CO PV diagrams (not shown here).

The two-core structure, in CS and N_2H^+, observed in PER9 is similar to that found in PER6. Because the CS(2–1) line profiles are blue-asymmetric we used only $N_2H^+(1–0)$ to search for velocity gradients across core B. Table 3 clearly shows that the velocity gradients observed towards the PER6, PER7 and PER9 cores are quite similar. The average direction among these cores (excluding B 1) is 53°, which is close to the direction of the velocity gradient observed in the large-scale molecular gas (41°).

4. Discussion

4.1. Pre-protostellar cores in the Perseus region

In Sect. 3.1 we have seen that in three cases we find evidence of an isolated CS core with no or very weak N_2H^+ emission. These are PER3-A, PER6-B and PER9-A. In PER3-A and PER9-A the CS(2–1) line profiles are blue-asymmetric, whereas in PER6-B this asymmetricity is best observed when the average of the spectra over the extent of the core is taken. The blue-asymmetry of the CS spectra suggests the presence of an infall velocity field in these three cores. If we apply the simple analytical model of Myers et al. (1996) to the mean spectrum in all three cores (for consistency) we find the infall velocities shown in Table 4. The velocity gradients observed towards these regions (see Table 3) are unlikely to mimic blue-asymmetric average line profiles in PER3-A and PER9-A, where the blue-asymmetry is observed in several CS(2–1) spectra, as mentioned above. However, we cannot exclude that this is the case in PER6-B, where the blue-asymmetry is less evident in the individual spectra.

Another interesting feature is that in all three cases the CS core is found to have a nearby N_2H^+ core, showing a weaker CS emission and no blue-asymmetric spectra, as shown in Figs. 2, 6 and 8. In the CS cores, PER3-A, PER6-B and PER9-A, the N_2H^+ abundance is lower (or much lower, in PER3-A, see Table 6) than the average abundance calculated over all Perseus cores observed by us.

Table 4. CS/N_2H^+ cores associations. The first column lists the cores, the second column shows the ratio of the integrated intensities, the third column reports the distance between the two cores and the fourth column shows the infall velocities. The cores S68NW and S68N in Serpens are included for comparison.

Core	$\frac{\int T_a^\star(\mathrm{CS})\mathrm{d}v}{\int T_a^\star(\mathrm{N_2H^+})\mathrm{d}v}$	Distance [pc]	$V_{\rm in}$ [km s^{-1}]
PER3-A	>55	0.32	0.13
PER3-B	1.29	–	–
PER6-B	>22	0.15	0.01
PER6-A	2.96	–	–
PER9-A	>9.8	0.45	0.03
PER9-B	2.32	–	–
S68NW[(a)]	≃16	0.1	0.34
S68N[(a)]	≃4.9	–	0.01

[(a)] From Williams & Myers (1999).

The main features of these three cores are very similar to those found by Williams & Myers (1999) in the case of the contracting, starless core S68NW in the Serpens molecular cloud complex. S68NW is a CS core with little N_2H^+ emission and is located nearby (≃0.1 pc) to a protostar, S68N, with a stronger N_2H^+ emission peaked at the position of the 3 mm continuum. Both S68N and S68NW show double-peaked CS spectra, but only the N_2H^+-weak core, S68NW, shows blue-asymmetric CS line profiles. For comparison, in PER3-B, PER6-A and PER9-B the average CS line profiles are all single-peaked. Furthermore, in PER3 and PER6 the IRAS source is located inside the N_2H^+-strong cores (PER3-B and PER6-A) but is not coincident with the peak position.

Williams & Myers (1999) concluded in the case of S68N/S68NW that the cloud is forming a core (S68NW) while its already formed core (S68N) is still forming a star, implying that the formation of stars and cores in Serpens may substantially overlap in time (see also OT). Although there are differences between the cores described here and S68NW, the incidence of cores similar to S68NW in the Perseus region seems to support the overlapping star-forming scenario. The main difference is the substantially lower infall velocities observed in PER3-A, PER6-B and PER9-A as compared to S68NW (see Table 4). Because the [CS/NH_3] and [CS]/[N_2H^+] abundance ratios reflect the depletion of CS at late times (see, e.g., Bergin & Langer 1997; Aikawa et al. 2001) our results suggest that the N_2H^+-weak cores PER3-A, PER6-B and PER9-A are in a somewhat earlier evolutionary stage as compared to their companion cores, PER3-B, PER6-A and PER9-B. This possible scenario deserves further observations and study, in order to understand how such large differences can be generated in the evolutionary stages of nearby cores.

4.2. Physical parameters

Maps of the $N_2H^+(1–0)$ emission were extended at least to half-power, and we estimate the source diameter, D_s, as

$$D_s = 2\left[\left(\frac{A}{\pi}\right) - \left(d\,\frac{\theta_b}{2}\right)\right]^{0.5} \quad (1)$$

where A is the area within the half-maximum contour, θ_b is the FWHM beam diameter of the observations (54″), and d is the assumed distance to the Perseus complex (350 pc). Values for D_s are listed in Table 2. The average value of the source diameter for individual cores in our sample is $\langle D_s\rangle = 0.16 \pm 0.04$ pc, which is lower than the average value (0.22 ± 0.06 pc) found by LMG using their NH_3 maps. This discrepancy is a consequence of the larger beam size (88″) and the different cores considered in the work by LMG. On the other hand, the diameters of the individual cores are very similar to those found by CBMT.

We have then used the hyperfine structure (hfs, hereafter; see, e.g., Caselli et al. 1995) of the $N_2H^+(1–0)$ line and the hfs fitting program in CLASS[2] to determine LSR velocities (V_{LSR}), intrinsic line widths (Δv), total optical depths (τ_{tot}) and excitation temperatures (T_{ex}). The average values of these parameters, over the extent of each core, are listed in Table 5. When considering the mean properties of the cores, it is interesting to note that the mean line width, $\langle\Delta v\rangle = 0.39 \pm 0.08$ km s^{-1}, is consistent, within the errors, with that found by LMG (0.35 ± 0.05 km s^{-1}), despite all effects that may cause a lack of correlation between the properties of N_2H^+ and NH_3 (Benson et al. 1998, CBMT), which indicates that the emission of the two molecules comes from roughly the same physical region with similar turbulent line-widths.

Table 5 also lists the non-thermal line widths, $\langle\Delta v\rangle_{NT}$, after removal of the thermal contribution of N_2H^+ from $\langle\Delta v\rangle$. These non-thermal line widths, with a few exceptions, are each comparable to or less than the corresponding width of the velocity distribution of the molecule of mean mass, $\Delta v_{mol} = 0.47$ km s^{-1}, at a kinetic temperature of 11 K. Thus, the typical core in our sample has non-thermal motions comparable to or less than its thermal motions. PER3-B is the core with the greater turbulent motion and is probably a consequence of being in a state of turbulent infall (see Sect. 4.1).

The virial mass of each core has been calculated as:

$$M_{vir}(M_\odot) = 0.509\, d(\mathrm{kpc})\, \theta_s(\mathrm{arcsec})\, \Delta v^2_{mol}\left(\mathrm{km\,s^{-1}}\right) \quad (2)$$

where θ_s is the angular diameter of the source and Δv_{mol} is the full width at half maximum of the molecule of mean mass (2.33 amu)

$$\Delta v^2_{mol} = \Delta v^2 + 8(\ln 2)\, kT\left(\frac{1}{2.33} - \frac{1}{m_{N_2H^+}}\right) \quad (3)$$

where $m_{N_2H^+}$ is the mass of the N_2H^+ molecule (29 amu) and Δv is the intrinsic line width of the $N_2H^+(1–0)$ line, averaged over the core and listed in Table 5. The corresponding number density, n_{vir}, has been calculated assuming a uniform density spherical core with diameter given in Table 2. M_{vir} and n_{vir} are listed in Cols. (2) and (5) of Table 6, respectively. The average value of M_{vir} for individual cores is $5.6 \pm 1.7\ M_\odot$ and it is thus quite similar to that found by LMG ($5.0 \pm 4.0\ M_\odot$), though with a smaller scatter, and confirms their conclusion, i.e., the mean properties of the Perseus cores are intermediate between those of the Taurus and Orion A cloud complexes.

In Col. (3) of Table 6 we also list the masses of the N_2H^+ molecular gas calculated using the formula:

$$M_{cd} = d^2\, m_{N_2H^+} \int N_{N_2H^+}\, d\Omega \quad (4)$$

where $\int N_{N_2H^+}\, d\Omega$ is the molecule column density integrated over the region enclosed by the contour level at 50% of the peak value for each core, unless stated otherwise in Table 6, and $m_{N_2H^+}$ is the mass of the N_2H^+ molecule. Column (4) reports the N_2H^+ fractional abundance, $X(N_2H^+) = M_{cd}(N_2H^+)/M_{vir}$. The average value of $X(N_2H^+)$ for individual cores is $(5.9 \pm 2.1) \times 10^{-10}$, which is slightly larger, though consistent within the errors, than the average value (4×10^{-10}) found by CBMT for a smaller and different sample of Perseus cores. One can also see that for the PER3-A and PER9-A cores discussed in Sect. 4.1 the N_2H^+ abundance is less than 50% of the average value (although this difference also includes potential errors in the method used to determine the abundance), suggesting that in these cores the abundance of this molecule is unusually low.

Table 5. N_2H^+ map results: average values obtained with the multi-component (hfs) fit. τ_{tot} represents the sum of the peak optical depth of the seven hyperfine components. T_{ex} is the excitation temperature calculated assuming a main-beam efficiency $\eta_B = 0.45$.

Core	$\langle V_{LSR}\rangle$ [km s^{-1}]	$\langle\Delta v\rangle$ [km s^{-1}]	$\langle\Delta v\rangle_{NT}$ [km s^{-1}]	$\langle\tau_{tot}\rangle$	$\langle T_{ex}\rangle$ [K]
PER3-A[(a)]	6.32	0.38	0.36	0.1	–
PER3-B1	6.78	0.50	0.48	2.0	5.7
PER3-B2	7.18	0.50	0.48	3.0	5.4
PER3-C	7.30	0.45	0.43	3.2	3.9
PER4-A	7.43	0.33	0.31	3.7	5.2
PER4-B	7.52	0.33	0.31	4.0	5.0
PER4-C	7.56	0.35	0.33	5.0	5.5
PER4-D	7.70	0.35	0.33	3.5	5.5
PER5	8.20	0.32	0.29	3.4	4.3
PER6-A	5.86	0.36	0.33	2.9	6.0
PER6-B	4.98	0.34	0.31	2.0	4.1
PER7-A	6.47	0.41	0.39	6.4	4.3
PER7-B	6.73	0.41	0.39	3.7	4.3
PER7-C	6.61	0.34	0.28	4.8	4.3
PER9-A	6.53	0.36	0.33	4.7	3.7
PER9-B	6.82	0.38	0.33	6.1	4.0

[(a)] From hfs fit to position (44, 160).

[2] CLASS is part of the GILDAS software distributed by IRAM, Grenoble (F).

Table 6. Volume density and mass of the N_2H^+ and CS cores. The second column shows the virial masses of the cores, as calculated from N_2H^+; the third column lists the N_2H^+ masses obtained using the measured column densities; in the fourth column the abundance of N_2H^+ is shown, calculated using the values in the previous two columns; the fifth column shows the virial volume density corresponding to M_{vir}; the last two columns list the CS column density and the H_2 mass, respectively, calculated assuming $X(CS) = 4 \times 10^{-9}$. All masses have been calculated using the 50% contour level, unless stated otherwise.

Core	M_{vir} $[M_\odot]$	$M_{cd}(N_2H^+)$ $[\times 10^{-9}\ M_\odot]$	$X(N_2H^+)$ $[\times 10^{-10}]$	n_{vir} $[\times 10^4\ cm^{-3}]$	$M_{cd}(CS)$ $[\times 10^{-8}\ M_\odot]$	$M_{cd}(H_2)$ $[M_\odot]$
PER3-A[(b)]	8.7	3.0	3.4	2.1	5.2	13.1
PER3-B1	6.8	3.5	5.1	8.3	–	–
PER3-B2	8.6	8.2	9.5	4.9	–	–
PER3-B[(a)]	11.2	10.7	9.6	2.7	2.8	7.1
PER3-C	5.2	2.3	4.3	10.1	–	–
PER4-A	4.2	1.8	4.2	5.1	–	–
PER4-A,B[(c)]	–	–	–	–	5.1	12.8
PER4-B	3.3	3.0	9.1	8.3	–	–
PER4-C	8.0	7.2	8.9	1.7	4.8[(c)]	12.0[(c)]
PER4-D	4.9	3.3	6.7	4.0		
PER4-F[(b,c)]	–	–	–	–	2.1	5.2
PER5	4.9	4.5	9.0	4.0	3.1[(c)]	7.8[(c)]
PER6-A	5.3	3.7	6.9	5.2	–	–
PER6-B	3.1[(b)]	1.2[(b)]	3.9	10.4	1.8[(c)]	4.4[(c)]
PER7-A	6.6	3.8	5.8	4.5	1.7	4.3
PER7-B	5.8	2.8	4.8	5.7	1.3	3.3
PER7-C	3.8	1.5	4.0	7.3	0.5	1.3
PER9-A	5.7[(b)]	1.6[(b)]	2.8	4.7	3.5[(c)]	8.8[(c)]
PER9-B	4.7	3.1	6.6	7.1	0.1[(d)]	0.3[(d)]

[(a)] Using the N_2H^+ B_1 50% contour level and including the B_2 core in the area of emission.
[(b)] Using the integrated emission within the contour at 65%.
[(c)] Using the same optical depth as in PER3, $\tau = 4.6$.
[(d)] Using $\tau \simeq 1$.

5. Conclusions

We performed single-dish multi-line, multi-isotope wide-field imaging (up to about $20' \times 20'$) of the emission towards a sample of cores in the Perseus cloud complex using optically thick and optically thin molecular tracers. We also performed mosaic observations in the N_2H^+(1–0) line and in the adjacent 3 mm continuum with the OVRO interferometer. Our main goal was to study the structure and the dynamics of the cores and the distribution of the ambient molecular gas around the cores.

The $C^{18}O$(1–0) emission traces the spatial distribution of the ambient molecular gas and indicates that in the regions studied by us the densest gas is concentrated within two large filamentary structures roughly aligned along a NE–SW axis, one centered on the NGC 1333 region and another extending SW from the B 1 core, as also observed by LMG. The cores are located within these two ridges. The high-density gas was mapped using the $C^{32}S$(2–1) and N_2H^+(1–0) emission and, to a much lesser extent, by $C^{34}S$(2–1). These molecular tracers show several condensations but present otherwise a different appearance.

The Perseus region is characterized by the presence of multiple clumps along the line of sight and by several velocity fields that include infall, expansion, rotation and turbulence. We have analysed the large-scale motions, mainly using the $C^{18}O$(1–0) emission, and found that in the PER4/PER5 region the molecular gas in the SW and NE possess velocity gradients in opposite direction. The PER3 region is characterized by the presence of two or more clouds at different velocities.

In the PER4/PER5 and PER7 regions, where we can directly compare the large-scale and core velocity gradients, we find that they have the same sign and similar magnitudes. OT found that the angular momentum in the Serpens molecular cloud is roughly aligned with the average outflow axis. Therefore, the possibility that a link between the large-scale angular momentum and the pre-stellar cores exist must be further investigated.

Another interesting feature is the presence in Perseus of three isolated CS cores, showing blue-asymmetric line profiles and with no or very weak N_2H^+ emission, which are found to have a nearby (<0.45 pc) N_2H^+ core, showing a weaker CS emission and no blue-asymmetric spectra. Our hfs fits indicate that the differences in the N_2H^+ emission are not due to excitation effects and are rather suggesting different abundances. We have proposed that these differences could be due to different evolutionary stages; the timescales predicted by the chemical models for this type of chemical evolution is rather large ($\geq 10^6$ yrs, Bergin & Langer 1997; Aikawa et al. 2001), and it is

thus not yet clear how such different evolutionary stages can be generated in nearby cores. However, these cores are very similar to S68N/S68NW in Serpens (Williams & Myers 1999; OT) and reinforce an earlier conclusion (Williams & Myers 1999) that the formation of stars and cores may substantially overlap in time. If these findings will be confirmed, they can provide strong constraints on the cores evolutionary timescales and directly impact on the competing star formation theories.

Only one of the observed cores (PER5) was unambiguously detected in the 3 mm continuum with the OVRO interferometer. Emission from the N_2H^+(1–0) line was detected and mapped towards cores PER3, PER4 and PER5. The N_2H^+ intensity peaks observed with OVRO are not coincident with the peaks of the integrated emission measured with the single-dish, and only a small fraction of the single-dish flux is recovered with the interferometer, indicating that the emission of the diffuse, less dense gas is dominant compared to the emission coming from the localized denser regions imaged by OVRO. This is consistent with a scenario in which the observed cores represent relatively low density enhancements in the molecular cloud that still have to contract before being able to form stars.

Acknowledgements. Research at the Owens Valley Radio Observatory is supported by the National Science Foundation through NSF grant AST 96-13717. Star Formation research at Owens Valley is also supported by the NASA's Origins of Solar Systems program, grant NAGW-4030 and by the Norris Planetary Origins Project. During L.O.'s stay at the University of Puerto Rico this work was partially supported by the Puerto Rico Space Grant Consortium.

References

Aikawa, Y., Ohashi, N., Inutsuka, S., & Takakuwa, S. 2001, ApJ, 552, 639
Arce, H. G., & Goodman, A. A. 2003, Rev. Mex. Astron. Astrofis., 15, 123
Bachiller, R., & Cernicharo, J. 1986, A&A, 166, 283
Bachiller, R., & Cernicharo, J. 1990, A&A, 239, 276
Bachiller, R., Guilloteau, S., & Kahane, C. 1987, A&A, 173, 324
Bachiller, R., Menten, K. M., & del Rio-Alvarez, S. 1990, A&A, 236, 461
Benson, P. J., Caselli, P., & Myers, P. C. 1998, 506, 743
Bergin, E. A., & Langer, W. D. 1997, ApJ, 486, 316
Bergin, E. A., Alves, J., Huard, T., & Lada, C. J. 2002, ApJ, 570, L101
Borgman, J., & Blaauw, A. 1964, Bull. Astron. Inst. Netherlands, 17, 358
Caselli, P., Myers, P. C., & Thaddeus, P. 1995, ApJ, 455, L77
Caselli, P., Walmsley, C. M., Tafalla, M., Dore, L., & Myers, P. C. 1999, ApJ, 523, L165
Caselli, P., Benson, P. J., Myers, P. C., & Tafalla, M. 2002, ApJ, 572, 238
Goodman, A. A., Benson, P. J., Fuller, G. A., & Myers, P. C. 1993, ApJ, 406, 528
Gueth, F., Guilloteau, S., & Bachiller, R. 1996, A&A, 307, 891
Hartmann, L., Ballestreros-Paredes, J., & Bergin, E. A. 2001, ApJ, 562, 852
Jennings, R. E., Cameron, D. H. M., Cudlip, W., & Hirst, C. J. 1987, MNRAS, 226, 461
Ladd, E. F., Lada, E. A., & Myers, P. C. 1993, ApJ, 410, 168
Ladd, E. F., Myers, P. C., & Goodman, A. A. 1994, ApJ, 433, 117
Loren, R. B. 1976, ApJ, 209, 466
Motte, F., André, Ph., & Neri, R. 1998, A&A, 336, 150
Myers, P. C., Mardones, D., Tafalla, M., Williams, J. P., & Wilner, D. J. 1996, ApJ, 465, L133
Olmi, L., & Testi, L. 2002, A&A, 392, 1053
Palla, F., & Stahler, S. 2000, ApJ 540, 255
Sandell, G., & Knee, L. B. G. 2001, ApJ, 546, L49
Scoville, N. Z., Carlstrom, J. E., Chandler, C. J., et al. 1993, PASP, 105, 1482
Shu, F. H., Adams, F. C., & Lizano, S. 1987, ARA&A, 25, 23
Testi, L., & Sargent, A. I. 1998, ApJ, 508, L91
Testi, L., Sargent, A. I., Olmi, L., & Onello, J. S. 2000, ApJ, 540, L53
Warin, S., Castets, A., Langer, W. D., Wilson, R. W., & Pagani, L. 1996, A&A, 306, 935
Williams, J. P., & Myers, P. C. 1999, ApJ, 518, L37